# ARTICLE IN PRESS

YNIMG-08858; No. of pages: 9; 4C:

NeuroImage xxx (2011) xxx-xxx



Contents lists available at SciVerse ScienceDirect

## NeuroImage

journal homepage: www.elsevier.com/locate/ynimg



# Identification of cortical lamination in awake monkeys by high resolution magnetic resonance imaging

Gang Chen a,b,c, Feng Wang b,c, John C. Gore b,c,d,e,f, Anna W. Roe a,b,c,e,\*

- <sup>a</sup> Department of Psychology, Vanderbilt University, Nashville, TN 37203, USA
- <sup>b</sup> Vanderbilt University Institute of Imaging Science, Vanderbilt University, Nashville, TN 37235, USA
- <sup>c</sup> Department of Radiology and Radiological Sciences, Vanderbilt University, Nashville, TN37235, USA
- <sup>d</sup> Department of Physics and Astronomy, Vanderbilt University, Nashville, TN 37235, USA
- <sup>e</sup> Department of Biomedical Engineering, Vanderbilt University, Nashville, TN 37235, USA
- f Department of Molecular Physiology and Biophysics, Vanderbilt University, Nashville, TN 37235, USA

#### ARTICLE INFO

### 12 Article history:

**Q1**3

10

11

15

16

13 Received 27 May 2011 14 Revised 10 October 2011

Accepted 25 October 2011

Available online xxxx

# 20 Keywords:

21 High resolution MRI

22 MR microscopy

23 Non-human primate

24 Awake

25 Visual cortex

26 V1

47 46

48

49

50

51

52 53

54

55 56

57

59

60

61

62 63

27 Extrastriate cortex

#### ABSTRACT

Brodmann divided the neocortex into 47 different cortical areas based on histological differences in laminar myeloarchitectonic and cytoarchitectonic defined structure. The ability to do so *in vivo* with anatomical magnetic 29 resonance (MR) methods in awake subjects would be extremely advantageous for many functional studies. 30 However, due to the limitations of spatial resolution and contrast, this has been difficult to achieve in awake 31 subjects. Here, we report that by using a combination of MR microscopy and novel contrast effects, cortical layers 32 can be delineated in the visual cortex of awake subjects (nonhuman primates) at 4.7 T. We obtained data from 33 30-min acquisitions at voxel size of  $62.5 \times 62.5 \times 1000 \, \mu \text{m}^3$  (4 nl). Both the phase and magnitude components 34 of the  $T_2^*$ -weighted image were used to generate laminar profiles which are believed to reflect variations in 35 myelin and local cell density content across cortical depth. Based on this, we were able to identify six layers characteristic of the striate cortex (V1). These were the stripe of Kaes-Bechterew (in layer II/III), the stripe of Gennari 37 (in layer IV), the inner band of Baillarger (in layer V), as well as three sub-layers within layer IV (IVa, IVb, and 38 IVc). Furthermore, we found that the laminar structure of two extrastriate visual cortex (V2, V4) can also be 39 detected. Following the tradition of Brodmann, this significant improvement in cortical laminar visualization 40 should make it possible to discriminate cortical regions in awake subjects corresponding to differences in 41 myeloarchitecture and cytoarchitecture.

© 2011 Published by Elsevier Inc. 43

#### Introduction

The discovery of the stripe of Gennari (Gennari, 1782) in fresh visual cortical tissue was the first indication of lamination in the cerebral cortex. Over a century later, this lamination was formalized by Brodmann who divided the cortex of non-human primates into six layers (Brodmann, 1905) and, on the basis of distinct cytoarchitectural profiles (cell density, type, and size revealed by Nissl stains), delineated 43 separate areas in human neocortex (Brodmann, 1909). Cortical areas defined in this way have been found to correlate with specific functional specializations as determined by functional imaging in human subjects (Bridge et al., 2005; Geyer et al., 2011; Hinds et al., 2008; Sigalovsky et al., 2006) as well as electrophysiological and imaging in non-human primates.

A second way of differentiating cortical areas and layers is based on the pattern of myelinated fibers or myeloarchitectonic analysis (Braak, 1980). One well known myeloarchitectonic landmark is the stripe of

1053-8119/\$ – see front matter © 2011 Published by Elsevier Inc. doi:10.1016/j.neuroimage.2011.10.079

Gennari, a 280 µm thick (von Economo and Koskinas, 1929) myelin- 64 dense band, actually visible to the naked eye, located in the middle of 65 gray matter within the striate cortex (V1) (Valverde, 1985). This myelin 66 dense layer, which varies in thickness across cortical areas, is actually 67 found in all parts of the cortex (Baillarger, 1840) and has been used to 68 identify over thirty areas (Smith, 1907). Cortical layers and boundaries 69 of cortical areas defined by detailed myeloarchitectonic analysis have 70 coincided closely with those of Brodmann's cytoarchitectonic layers 71 and areas (Nieuwenhuys et al., 2008; Vogt and Vogt, 1919, 1954).

With advances in magnetic resonance (MR) imaging techniques, it is 73 possible to reveal detailed structural features in living subjects based on 74 variations in their intrinsic magnetic resonance properties such as 75 proton density and relaxation times. High resolution MR studies in 76 humans have succeeded at detecting the stripe of Gennari at 1.5 T 77 (Clark et al., 1992; Eickhoff et al., 2005; Walters et al., 2003). However, 78 due to the usual relatively low ratio between the in-plane resolution 79 and the width of the stripe of Gennari, partial volume effects lead to a 80 stripe with patchy appearance and fuzzy borders. The spatial resolution 81 in MR imaging is limited by multiple factors including the signal and contrast to noise ratios and the gradient strengths used (Callaghan et al., 83 1994). The signal per voxel decreases linearly with the reduction of 84

Please cite this article as: Chen, G., et al., Identification of cortical lamination in awake monkeys by high resolution magnetic resonance imaging, NeuroImage (2011), doi:10.1016/j.neuroimage.2011.10.079

<sup>\*</sup> Corresponding author at: Department of Psychology, Vanderbilt University, 301 Wilson Hall, 111 21st Avenue South, Nashville, TN 37203, USA. Fax: +1 615 343 8449. E-mail address: Anna.Roe@vanderbilt.edu (A.W. Roe).

87 88

89

90

91 92

93

94

95

96

97 98

99

100

101

102

103

104

105

106

107

108

109

110

111

113

114

115

116

117

118

119

120

121

122

123

124

125

126

127 128

129

130

131

132

134

135

136

137

138

voxel volume but increases with magnetic field strength, and decreases with coil size and signal bandwidth (Mansfield and Morris, 1982). Therefore, MR images can have similar signal to noise ratio (SNR) at higher spatial resolution in higher magnetic fields by using smaller coils. The ability to detect the stripe of Gennari generally improves with improved in-plane resolution (Barbier et al., 2002; Bridge et al., 2005; Carmichael et al., 2006) and by using thinner slices (Trampel et al., 2011; Turner et al., 2008), partly because this reduces the effects of partial volume averaging. Moreover, several groups have suggested that some contrast mechanisms (e.g. magnitude and phase changes in  $T_2^*$ -weighted imaging) are more favorable at high field than conventional MR contrasts (e.g.  $T_1$  and  $T_2$ ) and are more able to separate gray matter and white matter (Abduljalil et al., 2003; Duyn et al., 2007; Haacke et al., 2004).

Recent studies show that MR imaging in vivo can achieve spatial resolutions of better than 100 µm and that MR images acquired at such resolution in living animals can differentiate multiple cortical layers in mice (Boretius et al., 2009); moreover, additional myelinated structures outside the stripe of Gennari can apparently be detected within V1 of non-human primates (Goense and Logothetis, 2006; Goense et al., 2007). However, high resolution MR imaging at  $100 \times 100 \,\mu\text{m}^2$  in-plane resolution (or higher) has thus far been achieved primarily in anesthetized subjects. Compared with scanning in anesthetized subjects, the two main challenges facing improved spatial resolution in awake subjects are head-related motion blurring and the relatively short scan time. A combination of extensive training, specially designed training paradigms, and customized head-fixation may help overcome these problems (Chen et al., 2011). Here, we demonstrate the ability to reveal fine brain microstructure beyond the stripe of Gennari by high spatial resolution MR methods in awake behaving non-human primates at 4.7 T, a method we term 'MR microscopy' (Benveniste and Blackband, 2002). This will be the basis for addressing the correlation between cortical layers as well as laminar specific functional activation in awake subjects (Geyer et al., 2011; Trampel et al., 2011) and will be a useful approach for distinguishing cortical areas in such studies.

#### Material and methods

MR imaging data acquisition

MR images were acquired using a Varian 4.7 T vertical MR scanner (Varian Inc., Palo Alto, CA) with a 2-cm surface coil. Our results are obtained from two Macaque monkeys (*Macaca mulatta*) scanned on multiple sessions. All procedures conformed to the guidelines of the National Institute of Health and were approved by the Institutional Animal Care and Use Committee of Vanderbilt University. Before imaging, animals were implanted with MR-compatible headposts under general anesthesia (1–2% isoflurane). Monkeys were then placed in the vertical bore and trained to perform a continuous fixation task with fluid reward every 20 s throughout the scan.  $T_2^*$ -weighted gradient-echo images were acquired (repetition time = 200 to 350 ms, flip angle = 30° to 45°, echo time = 12 to 40 ms, in-plane resolution = 62.5 × 62.5  $\mu$ m<sup>2</sup> to 250×250  $\mu$ m<sup>2</sup>). Each scanning session consisted of up to five 30-min high resolution anatomical runs.

Data analysis

Images were reconstructed and analyzed using Matlab (Mathworks, Natric, MA) without zero filling and spatial filtering. The real (r) and imaginary (i) components of complex MR signals were used to calculate the magnitude (M) and phase maps (P) as following:

$$M = \sqrt{r^2 + i^2} \tag{1}$$

 $P = \arctan\left(\frac{i}{r}\right) \tag{2}$ 

Phase maps were corrected for macroscopic magnetic field varia- 144 tions, which were estimated by an eight-order 2D polynomial function 145 after phase unwrapping (Duyn et al., 2007; Yao et al., 2009). 146

Relatively flat regions of interest were selected (Supplementary Fig. 147). The outer (dura/gray matter boundary) and inner borders (white/ 148 gray matter boundary) of a cortical area were determined by manual 149 segmentation. The distances of each voxel in the ROI to the outer 150 (Supplementary Fig. 1B) and inner borders (Supplementary Fig. 1C) 151 were calculated using a minimum distance algorithm (Schleicher 152 et al., 2000). The cortical thickness was defined as the sum of distances 153 to outer and inner borders. To compensate for variations in cortical 154 thickness, cortical depth (Supplementary Fig. 1D) is normalized as 155 follows:

$$Cortical\ Depth(\%) = \frac{Distance_{Outer\ border}}{Distance_{Outer\ border} + Distance_{Inner\ border}} \times 100 \quad (3)$$

Profiles of cell body and myelin density in V1 were interpreted based 159 on the literature (Billings-Gagliardi et al., 1974; Brodmann, 1905; Peters 160 and Sethares, 1996). The histological sections were smoothed mildly by 161 a moving average filter with span of 5% of the cortical depth. All profiles were z-normalized to account for the difference among modalities (Boretius et al., 2009; Eickhoff et al., 2005). Areal borders between 164 visual cortical areas were based on published atlases (Saleem and 165 Logothetis, 2007).

The relative displacement between two structural images was  $^{167}$  estimated by an in-plane rigid body model. The index of motion  $^{168}$   $^{169}$   $^{16$ 

$$Displacement = \sqrt{Tran_x^2 + Tran_y^2}$$
 (4)

The contrast-to-noise ratio between gray matter (GM) and white 173 matter (WM) was calculated as the signal difference between GM and 174 WM divided by the noise in the background.

172

Results 176

Effect of imaging parameters on contrast and quality of high resolution 177 images

The in-plane sizes of voxels used in this study are summarized in 179 Fig. 1A. The smallest voxel we employed was an in-plane size of 180  $62.5 \times 62.5 \,\mu\text{m}^2$  (red square), which is 0.04% and 0.25% of the in-plane 181 voxel size used in most human  $(3000 \times 3000 \,\mu\text{m}^2)$ , white square) and 182 awake non-human primate  $(1250 \times 1250 \,\mu\text{m}^2, \text{gray square})$  functional 183 MR imaging studies. This small size increases our ability to reveal fine 184 anatomical structures. The T<sub>2</sub>\*-weighted magnitude images of a sagittal 185 slice in an awake monkey at different in-plane resolutions with the 186 same slice thickness of 2 mm are shown in Figs. 1B-D. These anatomical 187 runs were collected in the same session and lasted up to 15 min. At in- 188 plane voxel size of  $250 \times 250 \,\mu\text{m}^2$  (Fig. 1B), the gray matter and white 189 matter can be discriminated. In Fig. 1C, the stripe of Gennari (yellow 190 arrow), which is about 200 µm thick in monkey V1, is detectable in 191 the middle of gray matter at in-plane resolution of  $125 \times 125 \,\mu\text{m}^2$ . By 192 further increasing the spatial resolution to  $62.5 \times 62.5 \,\mu\text{m}^2$  (Fig. 1D), 193 small intracortical veins (orange arrows) within the gray matter are dis-194 tinguishable. Dura and pial veins can be seen at the surface of some cortical areas.

To further improve the quality of the structural image, we oriented 197 the imaging plane perpendicular to the cortical surface and used a 198 slice thickness of 1 mm (Trampel et al., 2011; Turner et al., 2008) to 199 minimize any partial volume effect. Fig. 2A shows the averaged results 200 of three 30-min runs with adjusted slice parameters. The dura (yellow 201 line in Fig. 2B) and pial veins (red dots) can be clearly detected at the

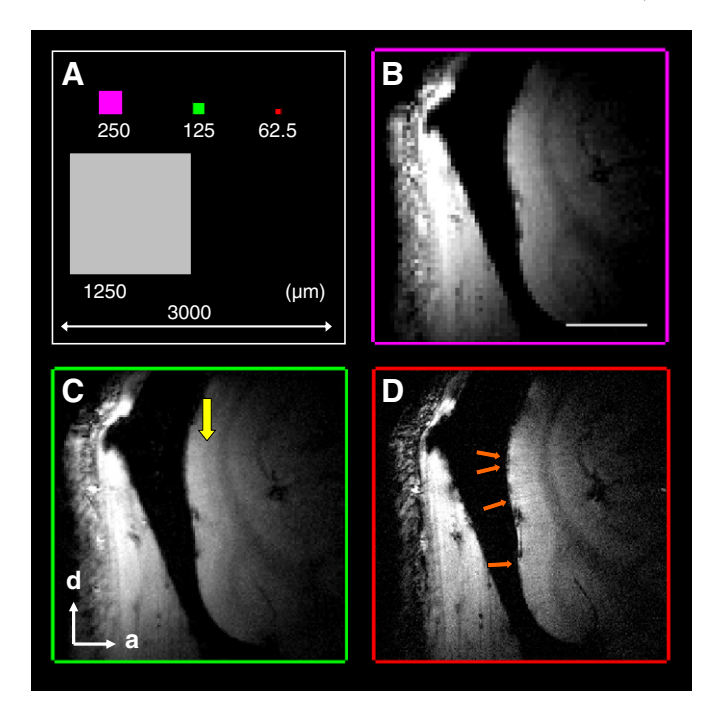


**Fig. 1.** Influence of in-plane resolution on image quality. (A) The relative in-plane size of voxels used in this and other MR imaging studies. (B–D) The  $T_2^*$ -weighted images (slice thickness 2 mm) from the visual cortex of an awake monkey as a function of in-plane resolution. The in-plane resolutions are  $250\times250\,\mu\text{m}^2$ ,  $125\times125\,\mu\text{m}^2$ , and  $62.5\times62.5\,\mu\text{m}^2$  for (B), (C), and (D), respectively. The stripe of Gennari (yellow arrow in C) and cortical veins (orange arrows in D) are detectable. Scale bar in (B): 5 mm. d, dorsal; a, anterior. (For interpretation of the references to colour in this figure legend, the reader is referred to the web version of this article.)

cortical surface. Principal veins (orange lines), which run through the gray matter (Duvernoy et al., 1981), had lower signals and higher contrast than those in the thicker slice shown in Fig. 1D. The contrast between gray matter (GM) and white matter (WM) regions was high in most cortical areas. Due to the use of a 2-cm surface coil for both transmission and reception, the sensitivity of MR signal decreases with distance to the coil. In Fig. 2C, we plotted the GM-WM contrast-to-noise ratio (CNR) against the cortical depth. As expected, the CNRs were the greatest at the cortical surface (around 20:1) and gradually decreased with depth. Even in cortical areas located 2 mm from the surface, the CNRs were about 10:1, a ratio still sufficient for clearly discriminating GM from WM.

203

204

205

206

207

208

209

210 211

212

213

214

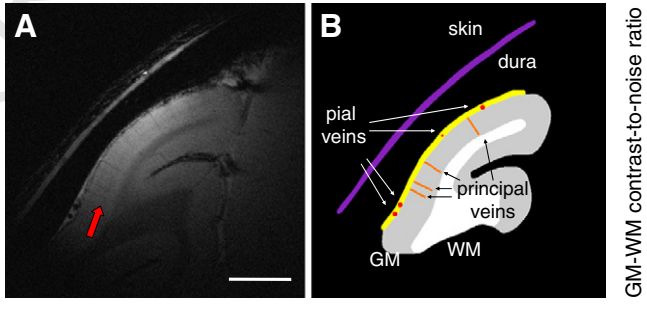
215 216 The other important parameter to consider is the echo time (TE), the delay between the RF excitation and data acquisition, used in the gradient-echo sequence. The optimal contrast between GM and WM

is usually achieved when a TE between T2\* values of GM and WM is 218 used. To determine the optimal TE for best contrast within GM, we test- 219 ed TE values of 20, 30, and 35 ms. We plot the z-normalized profiles of 220 magnitude (Fig. 3A) and phase (Fig. 3B) acquired at these three TEs 221 against the cortical depth. The magnitude profile obtained with the 222 shortest TE (20 ms, red line) has two dips, at about 25% and 50% cortical 223 depth (Fig. 3A). Dips are also observed at TEs of 30 ms (green line) and 224 35 ms (blue line). The shapes of these three magnitude profiles are very 225 similar. In contrast, the phase profiles differ as a function of TE (Fig. 3B). 226 At superficial depths (<50% cortical depth) the phase tends to be great- 227 est for 35 ms TE, smaller for 30 ms TE, and smallest for 20 ms TE, while 228 at greater depths (e.g. >50% cortical depth) the phase is greatest for 229 20 ms TE, less for 30 ms TE, and least for 35 ms TE. We relate these 230 depth-related differences in TE profile to laminar divisions within the 231 neocortex: the supragranular, granular, and infragranular layers 232 (roughly 0-33%, 33-66%, and 66-100% cortical depth, respectively). 233 These three anatomically defined laminar divisions are defined based 234 on relative location to granular layer IV and each occupies roughly 235 one-third of the cortical depth. All three phase profiles had a peak within the granular layer. Such peak in the middle of the gray matter is the 237 only one for the profile of 20 ms TE (red line). No clear peak could be 238 found within either supragranular or infragranular layers. When the 239 TEs are lengthened to 30 ms (green line) and 35 ms (blue line), the con- 240 trasts between the supragranular and the granular layers decreased and 241 the contrasts between the granular and infragranular layers increased. 242 At a TE of 30 ms, we found these two contrasts were almost the same 243 and that, in addition to the one in the granular layer, there were two ad- 244 ditional peaks within the supragranular and infragranular layers. Thus, 245 at TE of 30 ms, we find balanced contrasts between the supragranular 246 and infragranular layers and therefore maximal structural contrast 247 within GM; this TE value is close to the T<sub>2</sub>\* value of gray matter previ- 248 ously reported at 4.7 T (Pfeuffer et al., 2004). 249

Influence of head motion on image quality of MR microscopy in awake 250 subjects 251

A major challenge in MR microscopy (Benveniste and Blackband, 252 2002) and high resolution structural imaging in awake subjects 253 (Duyn, 2010) is the problem of subtle head motion. We have previously 254 shown that, with proper training paradigms and customized head fixa-255 tion, head displacements of awake monkeys can be limited to less than 256 100  $\mu$ m (Chen et al., 2011; Lu et al., 2010; Tanigawa et al., 2010). Here, 257 we examined whether the high resolution structural images collected 258 in behaving monkeys with in-plane resolution of  $100 \times 100 \ \mu$ m<sup>2</sup> or 259 higher were contaminated by head motion.

Fig. 4A shows the magnitude map from a 30-min anatomical run, 261 which had an in-plane resolution of  $100 \times 100 \,\mu\text{m}^2$  and thickness of 262 1 mm from an awake monkey. Although the duration of the scan was 263



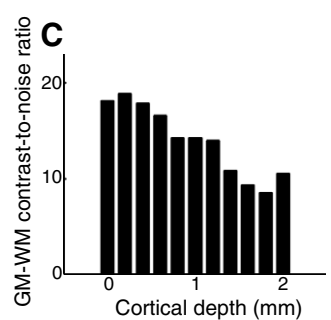


Fig. 2. High resolution structural image in the awake monkey V1. (A) A high resolution structural image with in-plane resolution of  $62.5 \times 62.5 \,\mu\text{m}^2$  and slice thickness of 1 mm shows fine anatomical structures of V1. The slice is oriented perpendicular to the cortical surface. The gray and white matter are clearly separable, and the stripe of Gennari (red arrow) can be seen in the middle of gray matter. (B) Illustration of anatomical structures. Skin and dura are marked as purple and yellow lines, respectively. Pial veins are indicated by red dots, and principal veins running through the gray matter are shown as orange lines. WM, white matter. GM, gray matter. Scale bar in (A): 5 mm. (C) The contrast-to-noise ratio between the gray matter and white matter plotted against the cortical depth. (For interpretation of the references to colour in this figure legend, the reader is referred to the web version of this article.)

Please cite this article as: Chen, G., et al., Identification of cortical lamination in awake monkeys by high resolution magnetic resonance imaging, NeuroImage (2011), doi:10.1016/j.neuroimage.2011.10.079

265

266

267

268

269

270

271

272

273 274

275

276

277 278

279

280

281

282 283

284

285 286

287 288

289

290

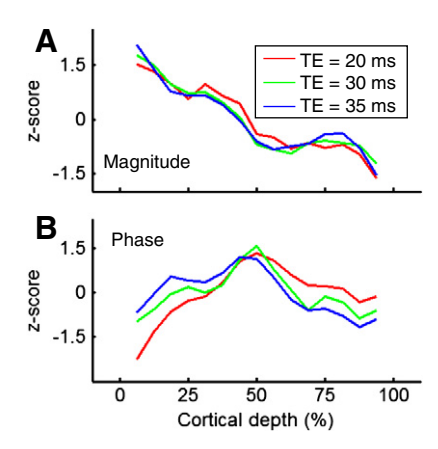


Fig. 3. Cortical depth profiles of T<sub>2</sub>\*-weighted images are a function of echo time (TE). The magnitude (A) and the phase (B) profiles of T<sub>2</sub>\*-weighted images. The average profiles at different echo time of 20 ms, 30 ms, and 35 ms are marked as red, green, and blue lines. Profiles are z-normalized and plotted against the distance from the cortical surface in percent of cortical depth for a better comparison. (For interpretation of the references to colour in this figure legend, the reader is referred to the web version of this article.)

one-third of the one presented in Fig. 2A, the GM-WM CNRs were sufficient to discriminate GM from WM. Dura (location of yellow line in Fig. 2B) could be clearly distinguished from the cortex. Draining veins on the cortical surface (gray arrows) and within lunate sulcus (black arrows) contain high concentration of deoxygenated hemoglobin, which are seen as dark spots in the T<sub>2</sub>\*-weighted image. If there were serious motion blur, images of principal veins, which have an average diameter of 80-120 µm (Duvernoy et al., 1981), would be wider and harder to detect. This was not the case. Several principal veins (white arrows), whose diameters were about 100 µm, were detected within the gray matter. A second run (Fig. 4B) acquired one hour later had the same duration, in-plane resolution, and thickness. All anatomical structures marked in Fig. 4A can be found, including the pial veins (gray arrows) and deep draining veins (black arrows). In this second run, principal veins (white arrows) were located at the same location and had similar diameter, indicating the average head motion between two runs is effectively well under 100 µm.

A rigid body registration between the images shown in Figs. 4A and B confirms this impression. The net displacement along the x-axis and v-axis were estimated to be 16 µm and 40 µm, respectively. Both displacements were less than half of the in-plane voxel size  $(100 \times 100 \,\mu\text{m}^2)$ . As shown in Fig. 4C, in well trained animals, we found only subtle head motion across anatomical runs (each run lasting 30 min). As seen in the distribution of relative displacement between runs, the average displacement was  $24 \pm 32 \,\mu m$  (mean  $\pm$  SD). The majority of displacements (>90%) were smaller than 50 µm. Those larger than 100 µm comprised less than 4%. As the influence of head movement within a session was small compared with the voxel size, 291 runs acquired in the same session can be averaged without significant 292 loss of structural detail.

The small head displacements between runs from the same session 294 (Fig. 4C) permitted temporal averaging of runs and provided improved 295 image quality without reduction in resolution. We obtained good repro- 296 ducible profiles from multiple runs within a session (Figs. 4A and B) and 297 even from sessions acquired two weeks apart (Figs. 5A and B). Main an-298 atomical markers in Fig. 5A, including pial veins (gray arrows), principal 299 veins on the cortical surface (white arrow) and within the lunate sulcus 300 (black arrow), and draining veins (white and gray stars) were repeated- 301 ly detected (Fig. 5B).

302

303

Laminar structure in V1 revealed by magnitude and phase maps

The signal-to-noise ratio of the acquired data increases with the 304 square root of the imaging time, so we attempted to maximize the 305 duration of each run and the number of runs. In a well trained monkey, 306 we are able to collect up to five 30-min runs from a single session. Data 307 from such a two and a half hour session are shown in Fig. 6: the 308 averaged magnitude (Fig. 6A) and phase (Fig. 6B) maps from a session 309 using the optimal TE of 30 ms, thickness of 1 mm, voxel volume of 310 10 nl  $(100 \times 100 \,\mu\text{m}^2 \text{ in-plane})$ , and flip angle of 30° are shown. 311 Comparison of the map in Fig. 6A (2.5-h run) with that in Fig. 4A 312 (30 min run) reveals that the SNR of the magnitude map was significantly improved. Not only are GM and WM readily distinguished, but 314 two bands can be detected in the middle of the gray matter: one band 315 which corresponds with the stripe of Gennari (black arrow) and anoth- 316 er between the first band and the outer border of the GM (white arrow). 317 Examination of the z-normalized magnitude profile with the cortical 318 depth further supports the existence of additional fine structure within 319 the GM (Fig. 6C, black line: average of five runs, circles: individual runs). 320 There are two dips in this profile located at approximately 20% (white 321 arrow) and 60% cortical depth (black arrow) which correspond to the 322 two dark bands seen in Fig. 6A. Note that variations between different 323 runs were small.

Variations with laminar depth were also observed in phase maps. 325 Variations in phase in T<sub>2</sub>\*-weighted images has been reported to be 326 related to the density of ferritin, which co-localizes with myelin in V1 327 (Fukunaga et al., 2010). Fig. 6B presents the results based on phase 328 data. Phase information from areas outside the cortex and cortical 329 regions with low SNR exhibit large variations (Duyn et al., 2007). The 330 cortical area within V1 shows relatively smooth variations after the 331 phase unwrapping and polynomial fitting procedures (see Experimen- 332 tal Procedures). In the middle of the gray matter in V1, a bright band 333 Q3 (white arrow) 200 to 300 µm in width is seen, likely indicating a band 334 of high myelin density corresponding to layer IVb (the stripe of 335 Gennari). A second bright band (black arrow) can be detected between 336 the first bright band and the GM-WM border with a thickness of 100 to 337

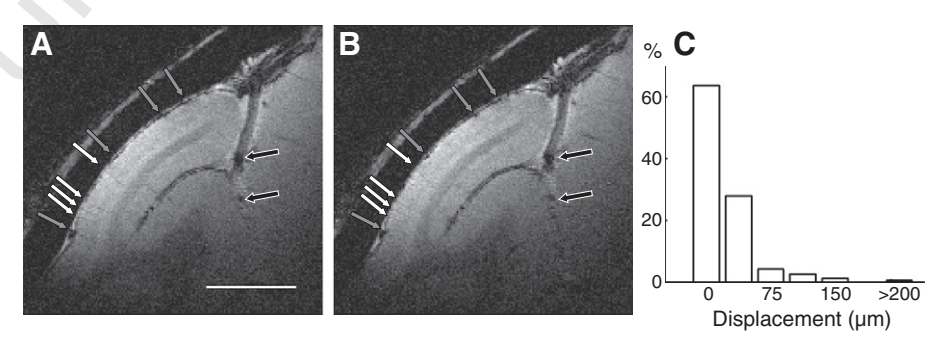
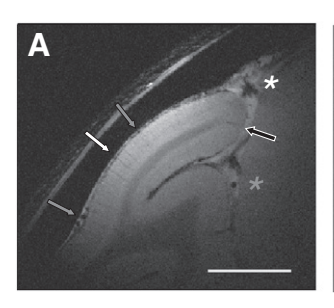


Fig. 4. Reproducibility of structural images within a session. (A and B) Structural images collected in two runs (30 min each) that were 1 h apart (slice thickness, 1 mm; in-plane resolution, 100×100 μm<sup>2</sup>). The locations of the pial veins (black and gray arrows) and principal veins within gray matter (white arrows) are the same. Scale bar: 5 mm. (C) The distribution of relative displacement between runs in the duration of 30 min (the length of a typical run).



338

339

340 341

342

343

344

345 346

347

348

349

 $350 \\ 351$ 

352

353

354

355

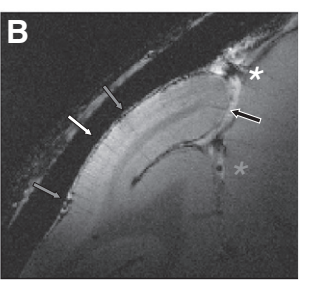


**Fig. 5.** Reproducibility of structural images between sessions. Structural images of V1 from the same awake monkey collected in two sessions that were 2 weeks apart are shown. (A) The in-plane voxel size was  $62.5 \times 62.5 \, \mu m^2$  and the thickness was 1 mm. (B) Inplane spatial resolution of  $100 \times 100 \, \mu m^2$  and a thickness of 1 mm. The location and shape of the pial veins within the lunate sulcus (white and gray stars) and on the cortical surface (gray arrows) are almost the same. The repeatable detection of principal veins within gray matter (gray and white arrows) further supports that the high resolution structural images from different sessions are highly reproducible. Scale bar: 5 mm.

200 µm. When plotted with respect to laminar depth, the phase profile (Fig. 6D) reveals two peaks (vertical white and black arrows). Again, phase values are fairly consistent across runs (black line: mean, circles: individual runs). A small third peak can also be seen at 20% cortical depth (gray arrow). Given these relative depths, we suggest these three bands correspond, respectively, to the stripe of Kaes-Bechterew (layer II/III) (gray arrow), the stripe of Gennari (white arrow) and the inner band of Baillarger (black arrow).

We observed similar laminar profiles within GM of V1 across slices obtained in all experiments. The mean magnitude profile (Fig. 7A) and phase profile (Fig. 7B) from all slices illustrates the consistency of these laminar profiles within gray matter. Previous studies have suggested that both magnitude and phase profiles reflect myelin density (Boretius et al., 2009; Duyn et al., 2007; Fukunaga et al., 2010), while the cell density may contribute mainly to the magnitude profile (Boretius et al., 2009). By combining the fluctuations indicated by these two profiles, we are able to infer laminar positions consistent with histologically determined cellular and myelin profiles. Based on

the magnitude profile, the two observed dips at around 60% and 90% 356 cortical depth (Fig. 7A, green arrowheads) are consistent with the location of the two high cellular and myelin density layers, layer IVc and 358 layer VI (Fig. 7F, blue arrowheads, based on (Billings-Gagliardi et al., 359 1974; Brodmann, 1905), replicated in Supplementary Fig. 2A). Based 360 on the phase profile, the three observed local peaks at around 20%, 361 50%, and 80% cortical depth (Fig. 7B, red arrowheads) overlap with 362 the location of highly myelinated bands, layers II/III, IVb, and V 363 (Fig. 7E, pink arrowheads, based on (Peters and Sethares, 1996), replicated in Supplementary Fig. 2B). From these combined profiles, layers 365 I and IVa can be inferred (Figs. 7C and D). Thus overall, seven laminated 366 structures in V1, including 3 within layer IV, can be identified (I, II/III, 367 IVa, IVb, IVc, V, and VI). As illustrated in Figs. 7C and D, lamina distinction from the MR microscopy approach (Fig. 7C) reveals a laminar 369 profile very similar to that obtained from cytoarchitectonic and mye- 370 loarchitectonic approaches (Fig. 7D). 371

Identification of cortical lamination in extrastriate visual cortex

In addition to the striate cortex (V1), we also examined the laminar 373 structure of two extrastriate visual cortex, V2 and V4, using MR micros-374 copy. Both cortical areas have distinct myeloarchitectonic structure 375 compared with V1. V2 has a relatively homogeneous and broad band 376 of fibers between layer IV and layer IV (Gattass et al., 1981). In contrast, 377 Q4 both the inner and outer bands of Baillarger in V4 are recognizable 378 (Gattass et al., 1988). A direct histological comparison of myelin stain-379 ing from these three cortical areas can be found in (Gattass et al., 380 1988) and is replicated as the Supplementary Fig. 3.

A MR image covering both V1 and V2 is shown in Fig. 8A. The relative 382 position of the surface coil on the head and parameters used in the scanning were similar as those in Fig. 6 except that the flip angle was in-384 creased from 30° to 45° to improve the SNR of MR signals from V2. A 385 dark band (pink arrow) can be detected in the middle of V2 from the 386 magnitude map (Fig. 8A). Its relative cortical depth is same as the stripe 387 of Gennari in V1 (white arrow) but with less contrast relative to gray 388 matter. In the phase map (Fig. 8B), one broad bright band (pink 389 arrow) is seen within V2, while there are two bright bands in V1 390

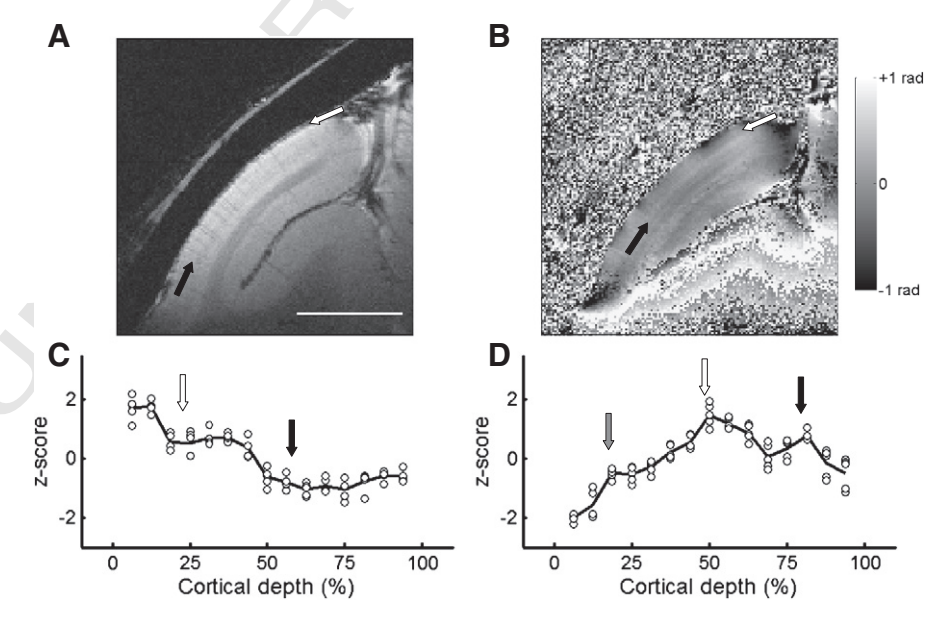


Fig. 6. Cortical profiles of magnitude and phase in V1. The magnitude (A) and phase (B) images of averaged results from five 30-min runs of a slice over V1 (slice thickness, 1 mm; in-plane resolution,  $100 \times 100 \,\mu\text{m}^2$ ). The stripe of Gennari (black arrow, layer IV) can be detected in (A). An additional dark layer can be found between the cortical surface and the layer IV (white arrow) from the magnitude map (A). From the phase map (B), a second bright layer (black arrow) exists between the layer IV (white arrow) and the white/gray matter border. (C) and (D) show the z-normalized profiles of magnitude and phase against cortical depth. The black lines indicate the averaged results, and circles represent results of individual runs. Locations of prominent laminar structures are indicated by arrows with the same color used in (A) and (B). A small third peak at 20% cortical depth can be detected in the phase profile (gray arrow). Scale bar in (A): 5 mm.

393

394

395

396 397

398

399

400

401

402

403

404

405

406

407

408 409

410

411

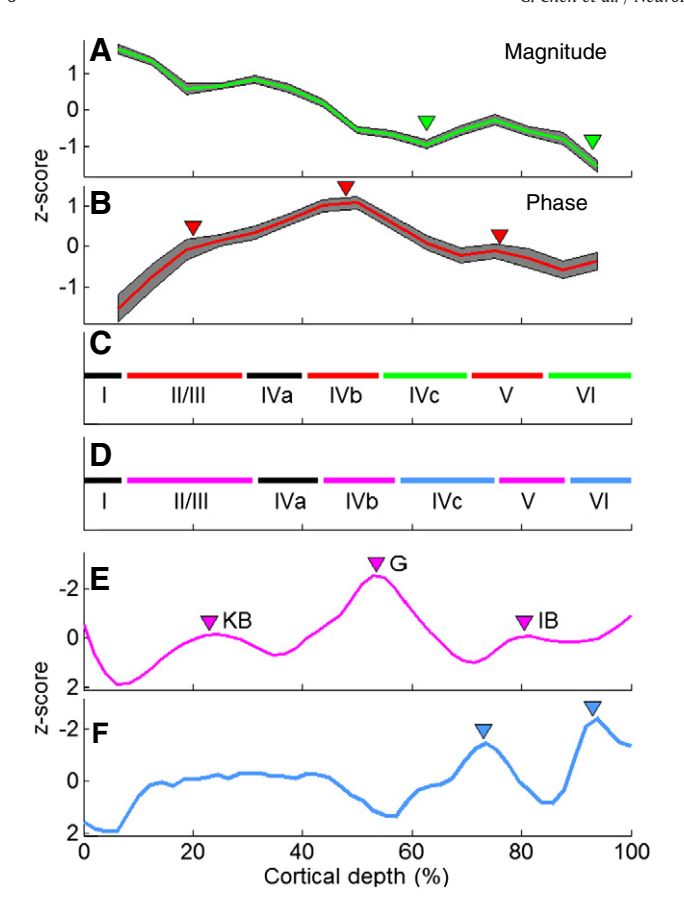


Fig. 7. Results from high resolution MRI reflect the myeloarchitecture and the cytoarchitecture of V1. The averaged results of magnitude (A) with dips marked (green triangles) from all runs and slices. The averaged results of phase profiles (B) with peaks marked (red triangles). The gray shadings represent the 95% confidence level in (A) and (B). (C) The laminar structure determined by MRI with peaks in phase profile (red lines) and dips in magnitude profile (green lines) marked. The laminar structure determined by conventional histology is shown in (D), Cell (E) and myelin densities (F) of V1 from literature are z-normalized and plotted against cortical depth with cortical areas of high õmyelin density marked by pink triangles and regions with high cell density marked by blue triangles. KB: the stripe of Kaes-Bechterew. G: the stripe of Gennari. IB: the inner band of Baillarger. The direction of v-axis of (D) and (E) is reversed for comparison. (For interpretation of the references to colour in this figure legend, the reader is referred to the web version of this article.)

(white arrows). The difference between the laminar structure of V1 and V2 is more prominent in the averaged profiles (Fig. 8E, V1, and Fig. 8F, V2). In contrast to V1, where there is a prominent peak in the phase profile near 50% and a smaller peak near 75% (Fig. 8E, green arrows), in V2 there is one broad peak (Fig. 8F, green arrow) in the phase profile (red line) centered around 60% cortical depth (Fig. 8F). This profile matches the description of the myeloarchitecture in V2 (Gattass et al., 1981, see Supplementary Fig. 3).

With MR microscopy, we found that V4 has a more complicated laminar structure than V2. As shown in Fig. 8D, two bright bands are seen in the phase map. The broader one is located in the middle of gray matter (red arrow), and a second bright layer (blue arrow) can be detected between the first band and the GM-WM border. Unlike V1 in which the deeper peak of the phase profile is stronger than the shallower one (red line, Fig. 8E), the two peaks in V4 are similar in size (red line, Fig. 8G). In the magnitude map (Fig. 8C), a dark layer (black arrow) in the middle of the gray matter is seen at a depth shallower (closer to the pial layer) than the stripe of Gennari.

In summary, we demonstrate that extrastriate cortical areas V2 and V4 have distinct laminar structure that can be differentiated by MR microscopy in awake monkeys.

#### Discussion

Laminar architecture in the visual cortex

The neocortex is defined by the presence of six cytoarchitectonic 414 layers (Billings-Gagliardi et al., 1974; Brodmann, 1905). In the striate 415 cortex (V1), these six layers are marked by specific characteristics. The 416 most superficial layer, molecular layer I, contains only few neurons. In 417 contrast, the external granular cell layer (layer II) contains a high densi- 418 ty of small pyramidal neurons as well as stellate neurons and the exter- 419 nal pyramidal layer (layer III) comprises somewhat larger pyramidal 420 cells similar in cell density to that of layer II. Within V1, the internal 421 granular layer IV can be further divided into a superficial portion (IVa) 422 containing many round cells, a cell-poor middle portion (IVb), and a 423 cell-rich deep portion (IVc). Below layer IVc, the internal pyramidal 424 cell layer (Layer V) is less dense and the deepest multiform layer VI con- 425 tains densely arranged spindle-shaped cells. Based on cell density, 426 layers I, IVb, and V are cell-poor zones while layers IVc, and VI are 427 cell-rich zones (blue lines in Fig. 7D and blue triangles in Fig. 7F). In 428 addition to cell type and density, several horizontal bands of myelina- 429 Q5 tion are prominent (pink lines in Fig. 7D and pink triangles in Fig. 7E) 430 providing a basis for myeloarchitecture. The outermost band is the 431 stripe of Kaes-Bechterew (Bechterew, 1891; Kaes, 1907), which is a 432 thin band of myelinated fibers (Fig. 7E, KB) located between layer II 433 and layer III (Braak, 1980). In the middle layers, the stripe of Gennari 434 (Figs. 6E, G) is a band of densely packed fibers, which is coincident 435 with layer IVb (Valverde, 1985). A third band with high myelin density 436 (inner band of Baillarger, IB in Fig. 7E) is located in layer V and is less 437 prominent and thinner than the stripe of Gennari.

419

413

454

Several intrinsic MR parameters, which have differential sensitivity 439 to cellular and myelin content, can be employed to reveal laminar architecture by MR imaging. Most high resolution MR histological studies in 441 awake subjects are based on T<sub>1</sub>-weighted images (Barbier et al., 2002; 442 Clare and Bridge, 2005; Eickhoff et al., 2005; Walters et al., 2003), an 443 approach which emphasizes the longitudinal relaxation process and 444 produces excellent contrast between gray and white matter. However, 445 the T<sub>1</sub> contrast within gray matter is relative low (Pfeuffer et al., 446 2004). At 7 T, the T<sub>1</sub> values for the stripe of Gennari were only 60 ms 447 shorter than the remaining gray matter layers within V1, a value 448 which is small compared with the variance of T<sub>1</sub> value (150 ms). Therefore, even with long scan times, no T<sub>1</sub>-contrast based study in awake 450 subjects was able to use in-plane voxel sizes less than  $300 \times 300 \,\mu\text{m}^2$ . 451 With a thickness of around 300 µm (von Economo and Koskinas, 452 1929), the stripe of Gennari was detected as a faint line with single 453 pixel width.

#### Phase and magnitude profiles

In the present study, we used MR contrasts from both the magnitude 456 and phase components of T2\*-weighted image with in-plane spatial 457 resolution of  $100 \times 100 \,\mu\text{m}^2$  or higher. The contrast in the phase component mainly originates from differences in magnetic susceptibility 459 between tissues arising mainly from differences in blood, iron and my- 460 elin density (Duyn et al., 2007). In V1, cortical iron co-localizes mainly 461 with myelin (Fukunaga et al., 2010), so the variation of the phase component in V1 reflects primarily the change of myelin density with cortical depth. In this study, the phase profile revealed three peaks at cortical 464 depths of 20%, 50%, and 80% (Fig. 7B). These depths coincide well with 465 the depths of cortical layers II/III, layer IVb, and layer V and, more specif- 466 ically, with the stripe of Kaes-Bechterew, stripe of Gennari, and the 467 inner band of Baillarger (compare phase profile (Fig. 7B) with myelin 468 profile (Fig. 7E)).

The second MR parameter we used to reveal laminar structure is 470 based on the magnitude component of the  $T_2^*$ -weighted image. The magnitude reflects variations in proton density (water content) and  $T_2^*$  472 values, which themselves depend on macromolecular content and 473

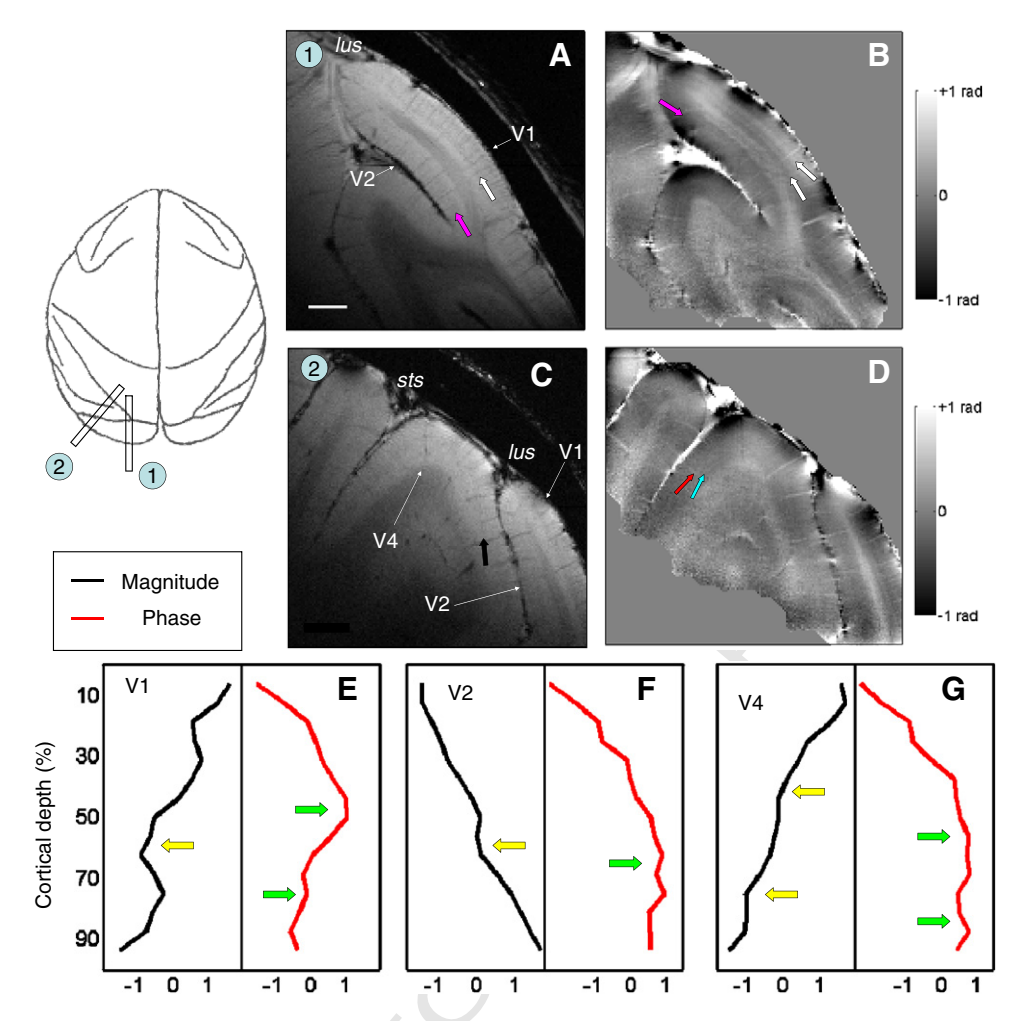


Fig. 8. MR structural images of extrastriate visual cortex. The magnitude (A) and phase (B) images of a parasagittal slice revealed V2 buried in the lunate sulcus (lus). Besides the stripe of Gennari (white arrow) in V1, a dark layer (pink arrow) can be found in the middle of V2 from the magnitude map (A). From the phase map (B), one bright layer exists in V2 (pink arrow) in additional to the two bright layers in V1 (white arrows). (C) and (D) An oblique slice that includes the portion of V4 that located between superior temporal sulcus (sts) and lus. Laminar structures within V4 (black arrows) can be found both from magnitude map (C) and phase map (D). The averaged results of magnitude (black lines) and phase profiles (red lines) from prestriate visual cortex of V1 (E), V2 (F), and V4 (G) are summarized. The peaks in phase profiles and dips in magnitude profiles are marked by green and yellow arrows, respectively. Both images were acquired with in-plane voxel size of  $100 \times 100 \ \mu m^2$ , thickness of 1 mm, and flip angle of 45°. Scale bar: 2 mm in (A). (For interpretation of the references to colour in this figure legend, the reader is referred to the web version of this article.)

variations in susceptibility. In our studies, using a short TR value and surface coil also withdraw a  $T_1$  dependent that varies with distance from the coil. When cell density increases the water content likely decreases and the voxel average  $T_1$  and  $T_2^*$  values also should be reduced. Additionally, myelin contains populations of protons that are essentially MR-invisible at long echo times used for imaging (Horch et al., 2011). It has been suggested that the contrast in  $T_2$ -weighted images reflect both myelin content and cell body density (Boretius et al., 2009; Yoshiura et al., 2000), although convincing evidence that directly links neural cell density to MR signal is still lacking. This may explain our finding that cell-rich layers (layers IVc, and VI) appear dark in the magnitude profile (Fig. 7A, green triangles). As shown in Fig. 7A, the heavily myelinated, relatively cell-sparse cortical layer IVb was visibly darker than the myelin-poor, cell-dense layer IVa. Thus, our results are consistent with known laminar structure and with localization of cell density and to myelination.

477

 In principle, the physical origins of MRI contrast and the fine cortical microstructure can be characterized more fully by quantitatively measuring values of  $T_1$ ,  $T_2$ , and  $T_2^*$ . However, this was not done in this study due to the limited duration of imaging sessions in awake subjects. In the future, direct links between MRI parameter maps and their histological basis can be obtained by using more myelin-specific measurements (Laule et al., 2007; Ou et al., 2009) or in correlative ex-vivo experiments that require sacrificing the animals, scanning the fixed

brain at very high resolution and then performing quantitative histolog-497 ical analysis on corresponding slices.

Using improved in-plane resolution of  $100 \times 100 \, \mu m^2$  or higher, we 499 have successfully delineated for the first time sub-layers within layer 500 IV. Magnitude profiles obtained with in-plane resolution up to 501  $240 \times 240 \, \mu m^2$  show a single dip in the middle of the gray matter 502 (Duyn et al., 2007). In this study, by acquiring images with fivefold-503 smaller volumes (58 nl vs. 10 nl), we found there were in fact two 504 dips in the magnitude profile. The locations of these dips were in the 505 middle of the gray matter, one corresponding to the highly myelinated 506 layer IVb and the second, about 150  $\mu$ m deeper than the first, corresponding to the high cell dense layer IVc. An alternative explanation 508 to the presence of this dip is that the magnitude profile reflects relatively denser vascular networks within layer IVc (Smirnakis et al., 2007; 510 Zheng et al., 1991), leading to relatively higher concentration of deoxygenated hemoglobin and shortening of  $T_2$ \* (Ogawa and Lee, 1990; 512 Schenck, 1992; Thulborn et al., 1982).

MR microscopy differentiates visual cortical areas in awake subjects 514 based on distinct laminar structure 515

In addition to V1 (striate cortex), there are more than 30 cortical 516 areas either dedicated to or associated with visual function in the 517

519 520

521

522

523

524

525 526

527

528

529

531

532

533

534

535

536

537

538

539 540

541

542

543

546

548

549

550

551

552

553

554

555

556 557

558

559

560 561

562

563

564

565

566

567

568

569

570

571

572

573

574

575

577

578

579

580

O6530

macaque monkey (Felleman and Van Essen, 1991). Most of them can be differentiated based on their myeloarchitecture. One example is shown in Supplementary Fig. 3 from (Gattass et al., 1981). This myelin stained slice illustrates the distinct laminar structures within striate area V1 and extrastriate areas V2 and V4. Both V1 and V4 have two bands of Baillarger. In V1, the outer one (red arrow, the stripe of Gennari) is more dense and thicker than the inner one (green arrow). On the contrary, the outer band (yellow arrow) has lower density of fiber compared to the inner band in V4 (pink arrow). Furthermore, the outer band of Baillarger in V4 is relatively broader than the stripe of Gennari. In comparison, V2 has only one relatively homogeneous fiber band between the typical two bands of Baillarger.

As we have discussed in the section Phase and magnitude profiles, the MR contrast of the phase component is heavily influenced by the myelin density. Hence, based on their different myeloarchitectonic profiles, V1, V2, and V4, should be readily distinguished by their phase profiles (red lines in Figs. 8E-G). Accordingly, we found that both V1 and V4 had two peaks in their phase profiles. The shallow peak is narrower in V1 than V4, and the difference between the amplitude of two peaks is relatively smaller in V4. As shown in Fig. 8F, the phase profile of V2 has only one broad peak covering cortical depths from 40% to 80%. Therefore, the laminar information from the phase component alone provides enough information to differentiate V1, V2, and V4. Interestingly, there are at least two dips in magnitude profiles of V1 and V4 while only one clear dip in V2 (black lines in Figs. 8E-G). The locations of dips are also different among the three cortical areas. Topics of our future research will include the origins of these differences and whether other extrastriate visual cortical areas (such as V3, MT, and FEF) can be differentiated using MR microscopy.

#### Other factors

Other improvements may have contributed to the success of high resolution imaging in awake subjects. First, to minimize partial volume effects, we purposely used imaging planes oriented perpendicular to the cortical surface. The shapes of the cortical surface in adjacent slices were used to verify the extent of orthogonality between the slice and the cortex. Thus, after proper adjustment, the long axis of a  $100 \times 100 \times 1000 \,\mu\text{m}^3$  voxel was almost perfectly parallel to cortical lamination. We found thicker slices (2 mm thick) were greatly influenced by partial volume effects (e.g. Fig. 1) as suggested by previous studies (Bridge et al., 2005; Carmichael et al., 2006), whereas thinner slices (<1 mm thick) had relatively low SNR at the in-plane resolution we used. One main disadvantage of our setup is that, due to the curvature of the brain, the fine anatomical structures of only a limited cortical area perpendicular to the slice can be revealed. The problem is more serious in MR microscopy of extrastriate cortex. For example, the fine structure of the cortex close to the V1/V2 border (Fig. 8B) and part of V4 folded within the superior temporal sulcus (Fig. 8C) is relatively indistinct. To reveal the cortical layers over a larger brain area, on gyri, or in sulci, isotropic voxels or thinner slices should be used (Trampel et al., 2011; Turner et al., 2008); this can be achieved by increasing the inplane resolution. Second, our monkeys which were exceptionally well-trained for the MR environment, performed with less than 100 µm head motion during scans (Chen et al., 2011). This permitted critical temporal averaging of runs and improved image quality without reduction in resolution (Fig. 6A). Third, we optimized MR sequence parameters to improve image quality. The choice of spatial resolution is the most important parameter for visibility of anatomical structure as suggested in Fig. 1 and in previous studies (Boretius et al., 2009). By acquiring MR images with high resolution, we eliminated the need to use interpolation to increase the nominal spatial resolution, a method which often introduces ringing artifacts (Clark et al., 1992; Wald et al., 2006). The other parameter we optimized was the TE. While previous studies showed that TE influences the phase contrast between gray and white matter (Duyn et al., 2007), here we found the TE also influences phase contrast within the gray matter (Fig. 3B). A prolonga- 582 tion of the TE improves the phase contrast between the superficial and 583 granular layers, although at a cost of poorer contrast between the gran- 584 ular and deeper layers (perhaps due to variance of  $T_2^*$  as function of cor- 585 tical depth in V1, (Fukunaga et al., 2010). Note that, at least in V1, the 586 selection of TE did not have significant influence on the magnitude con- 587 trast (Fig. 3A).

In sum, the use of phase and magnitude profiles to infer laminar 589 myelination and cell density patterns improves the ability to detect de- 590 tailed laminar cytoarchitecture in awake subjects using high resolution 591 MRI. These combined improvements revealed for the first time seven 592 cortical layers (including the three sub-layers within layer IV) in V1 of 593 awake subjects. Laminae separated by as little as 150 µm could be dis- 594 tinguished. In addition to that, we visualized two extrastriate cortical 595 areas with laminar structure distinct from V1. We predict that other 596 cortical regions may be differentiated anatomically in this way and 597 that such laminar signatures may be used to directly identify borders 598 between cortical areas in awake subjects. In combination with multi- 599 coil arrays (de Zwart et al., 2004; Goense et al., 2010; Wiggins et al., 600 2006), which cover larger areas with even better SNR and accelerated 601 image acquisition, it will hopefully be possible to conduct both high res- 602 olution anatomic and functional MR imaging within the same scanning 603 session. Such advances in MR methodology will provide highly needed 604 understanding of high spatial resolution relationships between brain 605 structure and function in awake subjects. Importantly, the application 606 of these methods for evaluation of cortical lamination changes in neurodegenerative disease and brain damage may lead to important break- 608 throughs in diagnosis and treatment.

#### Acknowledgments

This work was supported by NIH NS44375, EY11744, Vanderbilt 611 Vision Research Center, Vanderbilt University Center for Integrative & 612 Cognitive Neuroscience. The authors thank Chaohui Tang, Yanyan Chu, 613 and Mary R. Feutado for animal care; and Bruce Williams, Roger 614 Williams, Sasidha Tadanki, and Ken Wilkens for equipment and technical support. We are also grateful to Malcolm Avison for insightful 616 comments and suggestions.

610

618

#### Appendix A. Supplementary data

Supplementary data to this article can be found online at doi:10. 619 1016/j.neuroimage.2011.10.079. 620

#### References 621

Abduljalil, A.M., Schmalbrock, P., Novak, V., Chakeres, D.W., 2003. Enhanced gray and 622 white matter contrast of phase susceptibility-weighted images in ultra-high-field 623 magnetic resonance imaging. J. Magn. Reson. Imaging 18, 284–290. 624

Baillarger, J.G.F., 1840. Recherches sur la structure de la couche corticale des circonvolutions du cerveau. Mem. Acad. R. Med. 8, 149–183.

Barbier, E.L., Marrett, S., Danek, A., Vortmeyer, A., van Gelderen, P., Duyn, J., Bandettini, P., 627
 Grafman, J., Koretsky, A.P., 2002. Imaging cortical anatomy by high-resolution MR at 628
 3.0T: detection of the stripe of Gennari in visual area 17. Magn. Reson. Med. 48, 629
 735–738.

Bechterew, W., 1891. Zur Frage uber die ausseren Associationsfasern der Hirnrinde. 631 Neurol. Zentralbl. 10, 682–684. 632

Benveniste, H., Blackband, S., 2002. MR microscopy and high resolution small animal 633 MRI: applications in neuroscience research. Prog. Neurobiol. 67, 393–420. 634

Billings-Gagliardi, S., Chan-Palay, V., Palay, S.L., 1974. A review of lamination in area 17 635 of the visual cortex Macaca mulatta. J. Neurocytol. 3, 619–629.

Boretius, S., Kasper, L., Tammer, R., Michaelis, T., Frahm, J., 2009. MRI of cellular layers 637 in mouse brain in vivo. NeuroImage 47, 1252–1260.

Braak, H., 1980. Architectionics of the Human Telencephalic Cortex. Springer, Berlin.
 Bridge, H., Clare, S., Jenkinson, M., Jezzard, P., Parker, A.J., Matthews, P.M., 2005. Independent anatomical and functional measures of the V1/V2 boundary in human visual 641 cortex. J. Vis. 5, 93–102.

Brodmann, K., 1905. Beitrage zur histoloyische lokalization der Grosshirnrinde: Dritte 643
Mitteilung, Die Eindenfeldern der niederen Affen. J. Psychol. Neurol. 4, 177–226. 644
Brodmann, K., 1909. Vergleichende Lokalisationlehre der Grosshirnrinde. Johann Ambrosius Barth Verlag, Leipzig, Germany. 646

Please cite this article as: Chen, G., et al., Identification of cortical lamination in awake monkeys by high resolution magnetic resonance imaging, NeuroImage (2011), doi:10.1016/j.neuroimage.2011.10.079

714

717

718

719

726

731

732

733

734

736

737

738

739

742

743

745

746

747

748

749

750

751

752

753

757

761

765

766

767

768

769

770

771

744 Q10

735 **O9** 

Callaghan, P.T., Clark, C.I., Forde, L.C., 1994, Use of static and dynamic NMR microscopy to investigate the origins of contrast in images of biological tissues. Biophys. Chem. 50, 225-235.

647

648

649

650

651

652

653

654

655

657

658

659

660

661

662

663

664

665

666

667

669

670

671

672

673

674

675

676

677

678

679

680

681

682

683

684

685

686

687

688

689

690

691

692

693

694

695

696

697 698

699

700

701

702

703

704

705

706

707

708 709

774

**O8**668

O7656

- Carmichael D.W. Thomas D.L. De Vita F. Fernandez-Seara M.A. Chhina N. Cooper M., Sunderland, C., Randell, C., Turner, R., Ordidge, R.J., 2006. Improving whole brain structural MRI at 4.7 Tesla using 4 irregularly shaped receiver coils. Neuro-Image 32, 1176-1184,
- Chen, G., Wang, F., Dillenburger, B.C., Friedman, R., Chen, L., Gore, J., Avison, M.J., Roe, A.W., 2011. Functional magnetic resonance imaging of awake monkeys: some approaches for improving imaging quality. Magn. Reson. Imaging.
- Clare, S., Bridge, H., 2005. Methodological issues relating to in vivo cortical myelography using MRI. Hum. Brain Mapp. 26, 240-250.
- Clark, V.P., Courchesne, E., Grafe, M., 1992. In vivo myeloarchitectonic analysis of human striate and extrastriate cortex using magnetic resonance imaging. Cereb. Cortex 2, 417-424.
- de Zwart, J.A., Ledden, P.J., van Gelderen, P., Bodurka, J., Chu, R., Duyn, J.H., 2004. Signal-tonoise ratio and parallel imaging performance of a 16-channel receive-only brain coil array at 3.0 Tesla, Magn. Reson, Med. 51, 22-26.
- Duvernoy, H.M., Delon, S., Vannson, J.L., 1981. Cortical blood vessels of the human brain, Brain Res. Bull. 7, 519-579.
- Duyn, J.H., 2010. Study of brain anatomy with high-field MRI: recent progress. Magn. Reson. Imaging.
- Duyn, J.H., van Gelderen, P., Li, T.Q., de Zwart, J.A., Koretsky, A.P., Fukunaga, M., 2007. High-field MRI of brain cortical substructure based on signal phase. Proc. Natl. Acad. Sci. U. S. A. 104, 11796-11801.
- Eickhoff, S., Walters, N.B., Schleicher, A., Kril, J., Egan, G.F., Zilles, K., Watson, J.D., Amunts, K., 2005. High-resolution MRI reflects myeloarchitecture and cytoarchitecture of human cerebral cortex. Hum. Brain Mapp. 24, 206-215.
- Felleman, D.J., Van Essen, D.C., 1991. Distributed hierarchical processing in the primate cerebral cortex. Cereb. Cortex 1, 1-47.
- Fukunaga, M., Li, T.Q., van Gelderen, P., de Zwart, J.A., Shmueli, K., Yao, B., Lee, J., Maric, D., Aronova, M.A., Zhang, G., Leapman, R.D., Schenck, J.F., Merkle, H., Duyn, J.H., 2010. Layer-specific variation of iron content in cerebral cortex as a source of MRI contrast. Proc. Natl. Acad. Sci. U. S. A. 107, 3834-3839.
- Gattass, R., Gross, C.G., Sandell, J.H., 1981. Visual topography of V2 in the macaque. J. Comp. Neurol. 201, 519-539.
- Gattass, R., Sousa, A.P., Gross, C.G., 1988. Visuotopic organization and extent of V3 and V4 of the macaque. J. Neurosci. 8, 1831-1845.
- Gennari, F., 1782. Francisci gennari parmensis medicinae doctoris collegiati de peculiari structura cerebri nonnullisque eius morbis - paucae aliae anatom. Observat. Accedunt. Regio Typographeo, Parma, Italy.
- Geyer, S., Weiss, M., Reimann, K., Lohmann, G., Turner, R., 2011. Microstructural parcellation of the human cerebral cortex - from Brodmann's post-mortem map to in vivo mapping with high-field magnetic resonance imaging. Front. Hum. Neurosci. 5, 19.
- Goense, J.B., Logothetis, N.K., 2006. Laminar specificity in monkey V1 using highresolution SE-fMRI. Magn. Reson. Imaging 24, 381-392.
- Goense, J.B., Zappe, A.C., Logothetis, N.K., 2007. High-resolution fMRI of macaque V1. Magn. Reson. Imaging 25, 740-747.
- Goense, J., Logothetis, N.K., Merkle, H., 2010. Flexible, phase-matched, linear receive arrays for high-field MRI in monkeys. Magn. Reson. Imaging 28, 1183-1191.
- Haacke, E.M., Xu, Y., Cheng, Y.C., Reichenbach, J.R., 2004. Susceptibility weighted imaging (SWI). Magn. Reson. Med. 52, 612-618.
- Hinds, O.P., Rajendran, N., Polimeni, J.R., Augustinack, J.C., Wiggins, G., Wald, L.L., Diana Rosas, H., Potthast, A., Schwartz, E.L., Fischl, B., 2008. Accurate prediction of V1 location from cortical folds in a surface coordinate system. NeuroImage 39, 1585-1599.
- Horch, R.A., Gore, J.C., Does, M.D., 2011. Origins of the ultrashort-T2 1H NMR signals in myelinated nerve: a direct measure of myelin content? Magn. Reson. Med. 66, 24-31.
- Kaes, T., 1907. Die Grobhirnrinde des Menschen in ihren Maben und in ihrem Fasergehalt. Fischer, Iena.
- Laule, C., Vavasour, I.M., Kolind, S.H., Li, D.K., Traboulsee, T.L., Moore, G.R., MacKay, A.L., 2007. Magnetic resonance imaging of myelin. Neurotherapeutics 4, 460-484.
- Lu, H.D., Chen, G., Tanigawa, H., Roe, A.W., 2010. A motion direction map in macaque V2. Neuron 68, 1002-1013.

- Mansfield, P., Morris, P.G., 1982, NMR Imaging in Biomedicine, Academic Press, New York, 710 Nieuwenhuys, R., Voodg, J., Huijzen, C., 2008. The Human Central Nervous System, 4 ed. 711 Springer, Berlin,
- Ogawa, S., Lee, T.M., 1990. Magnetic resonance imaging of blood vessels at high fields: in 713 vivo and in vitro measurements and image simulation, Magn. Reson, Med. 16, 9-18.
- Ou, X., Sun, S.W., Liang, H.F., Song, S.K., Gochberg, D.F., 2009. The MT pool size ratio and 715 the DTI radial diffusivity may reflect the myelination in shiverer and control mice. 716 NMR Biomed, 22, 480-487.
- Peters, A., Sethares, C., 1996. Myelinated axons and the pyramidal cell modules in monkey primary visual cortex, J. Comp. Neurol, 365, 232-255
- Pfeuffer, J., Merkle, H., Beyerlein, M., Steudel, T., Logothetis, N.K., 2004. Anatomical and 720 functional MR imaging in the macaque monkey using a vertical large-bore 7 Tesla 721 setup. Magn. Reson. Imaging 22, 1343-1359. 722723
- Saleem, K.S., Logothetis, N.K., 2007. A Combined MRI and Histology Atlas of the Rhesus Monkey Brain in Stereotaxic Coordinates. Academic Press. 724 725
- Schenck, J.F., 1992. Health and physiological effects of human exposure to whole-body four-Tesla magnetic fields during MRI. Ann. N. Y. Acad. Sci. 649, 285-301.
- Schleicher, A., Amunts, K., Geyer, S., Kowalski, T., Schormann, T., Palomero-Gallagher, N., 727 Zilles, K., 2000. A stereological approach to human cortical architecture: identification 728 and delineation of cortical areas. J. Chem. Neuroanat. 20, 31-47. 729 730
- Sigalovsky, I.S., Fischl, B., Melcher, J.R., 2006. Mapping an intrinsic MR property of gray matter in auditory cortex of living humans: a possible marker for primary cortex and hemispheric differences. NeuroImage 32, 1524-1537.
- Smirnakis, S.M., Schmid, M.C., Weber, B., Tolias, A.S., Augath, M., Logothetis, N.K., 2007. Spatial specificity of BOLD versus cerebral blood volume fMRI for mapping cortical organization. J. Cereb. Blood Flow Metab.
- Smith, G.E., 1907. New studies on the folding of the visual cortex and the significance of the occipital sulci in the human brain. J. Anat. Physiol. 41, 198-207.
- Tanigawa, H., Lu, H.D., Roe, A.W., 2010. Functional organization for color and orientation in macaque V4. Nat. Neurosci. 13, 1542-1548.
- Thulborn, K.R., Waterton, J.C., Matthews, P.M., Radda, G.K., 1982. Oxygenation dependence 740 of the transverse relaxation time of water protons in whole blood at high field. 741 Biochim. Biophys. Acta 714, 265-270.
- Trampel, R., Ott, D.V., Turner, R., 2011. Do the congenitally blind have a stria of Gennari? First intracortical insights in vivo. Cereb. Cortex.
- Turner, R., Oros-Peusquens, A.M., Romanzetti, S., Zilles, K., Shah, N.J., 2008. Optimised in vivo visualisation of cortical structures in the human brain at 3 T using IR-TSE. Magn. Reson. Imaging 26, 935-942.
- Valverde, F., 1985. The organizing principles of the primary visual cortex in the monkey. In: Peters, A., Jones, E.G. (Eds.), Visual Cortex. Plenum, New York, pp. 207-257
- Vogt, C., Vogt, O., 1919. Allgemeinere Ergebnisse unserer Hirnforschung. J. Psychol. Neurol. 25, 279-461.
- Vogt, C., Vogt, O., 1954. Gestaltung der topistischen Hirnforschung und ihre Forderung durch den Hirnbau und seine Anomalien. J. Hirnforsch. 1, 1-46.
- von Economo, C.F., Koskinas, G.N., 1929. The Cytoarchitectonics of the Human Cerebral 754 Cortex. Oxford University Press, London. 756
- Wald, L.L., Fischl, B., Rosen, B.R., 2006. High-resolution and microscopic imaging at high field. In: Robitaille, P.M., Berliner, L. (Eds.), Ultra High Field Magnetic Resonance Imaging. Springer, New York, pp. 343-371.
- Walters, N.B., Egan, G.F., Kril, J.J., Kean, M., Waley, P., Jenkinson, M., Watson, J.D., 2003. In vivo identification of human cortical areas using high-resolution MRI; an approach to cerebral 760 structure-function correlation. Proc. Natl. Acad. Sci. U. S. A. 100, 2981-2986.
- Wiggins, G.C., Triantafyllou, C., Potthast, A., Reykowski, A., Nittka, M., Wald, L.L., 2006. 32-channel 3 Tesla receive-only phased-array head coil with soccer-ball element 763 geometry. Magn. Reson. Med. 56, 216-223.
- Yao, B., Li, T.Q., Gelderen, P., Shmueli, K., de Zwart, J.A., Duyn, J.H., 2009. Susceptibility contrast in high field MRI of human brain as a function of tissue iron content. Neuro-Image 44, 1259-1266.
- Yoshiura, T., Higano, S., Rubio, A., Shrier, D.A., Kwok, W.E., Iwanaga, S., Numaguchi, Y., 2000. Heschl and superior temporal gyri: low signal intensity of the cortex on T2-weighted MR images of the normal brain. Radiology 214, 217-221.
- Zheng, D., LaMantia, A.S., Purves, D., 1991. Specialized vascularization of the primate visual cortex. J. Neurosci. 11, 2622-2629.

772 773